Research Article | Vol. 30, No. 16 / 1 Aug 2022 / Optics Express 29030
Optics EXPRESS

Ultra-sensitive refractive index sensing enabled by a dramatic ellipsometric phase change at the band edge in a one-dimensional photonic crystal

FENG WU,[1,*] DEJUN LIU,[2,3] YAN LI,[1] AND HONGJU LI[4]

[1]School of Optoelectronic Engineering, Guangdong Polytechnic Normal University, Guangzhou 510665, China
[2]Department of Physics, Shanghai Normal University, Shanghai 200234, China
[3]Key Laboratory for Submillimeter Astrophysics, Shanghai Normal University, Shanghai 200234, China
[4]School of Physics, Hefei University of Technology, Hefei 230009, China
[*]fengwu@gpnu.edu.cn

Abstract: Surface plasmon polaritons (SPPs) and Bloch surface waves (BSWs) have been widely utilized to design sensitive refractive index sensors. However, SPP- and BSW-based refractive index sensors require additional coupling component (prism) or coupling structure (grating or fiber), which increases the difficulty to observe ultra-sensitive refractive index sensing in experiments. Herein, we realize dramatic ellipsometric phase change at the band edges in an all-dielectric one-dimensional photonic crystal for oblique incidence. By virtue of the dramatic ellipsometric phase change at the long-wavelength band edge, we design an ultra-sensitive refractive index sensor at near-infrared wavelengths. The minimal resolution of the designed sensor reaches 9.28×10^{-8} RIU. Compared with SPP- and BSW-based refractive index sensors, the designed ultra-sensitive refractive index sensor does *not* require any additional coupling component or coupling structure. Such ultra-sensitive refractive index sensor would possess applications in monitoring temperature, humidity, pressure, and concentration of biological analytes.

1. Introduction

Over the past decades, refractive index sensing has attracted the great interest of researchers due to its potential applications in monitoring temperature [1–3], humidity [4,5], pressure [6,7], and concentration of biological analytes [8–10]. It is known that optical resonances can be utilized to realize sensitive refractive index sensing [11–16]. Among them, two kinds of optical resonances have been utilized frequently, i.e., surface plasmon polaritons (SPPs) and Bloch surface waves (BSWs). for SPPs, electromagnetic waves are strongly enhanced around the interfaces between a metal layer and a dielectric layer [17,18]. Assisted by the unique resonant properties of SPPs, the resolution of refractive index sensors can be low as the order of 10^{-6} RIU (refractive index units) [19]. However, the dispersion relation of SPPs lies below the light cone, which indicates that SPPs *cannot* be directly excited by the electromagnetic waves incident from the air [17–19]. To achieve SPP-based sensitive refractive index sensing, additional coupling components (prisms [20–22]) or coupling structures (gratings [23,24] or fibers [25,26]) are required. For BSWs, electromagnetic waves are strongly enhanced around the surfaces of one-dimensional (1-D) photonic crystals (PhCs) [5,27–31]. Enabled by the unique resonant properties of BSWs, the resolution of refractive index sensors can be low as the order of 10^{-5} RIU [32,33]. Nevertheless, similar to SPPs, the dispersion relation of BSWs lies below the light cone [5,27–33]. To achieve BSW-based sensitive refractive index sensing, additional coupling components (prisms [34,35] or coupling structures (gratings [36–38]) are also required. Although SPPs and BSWs have

#469043 https://doi.org/10.1364/OE.469043
Journal © 2022 Received 27 Jun 2022; revised 13 Jul 2022; accepted 14 Jul 2022; published 22 Jul 2022

Optics EXPRESS

been widely utilized to achieve sensitive refractive index sensing, the requirement of additional coupling components or coupling structures increases the difficulty to observe ultra-sensitive refractive index sensing in experiments.

Recently, researchers utilized dramatic ellipsometric phase change of Tamm plasmon polaritons (TPPs) to achieve sensitive refractive index sensing [39–42]. Ellipsometric phase is the reflection phase difference between transverse magnetic (TM) and transverse electric (TE) polarized electromagnetic waves [43]. For TPPs, electromagnetic waves are strongly enhanced around the interfaces between a metal layer and a 1-D PhC [44–48]. Around the TPP wavelength at oblique incidence, the ellipsometric phase changes dramatically with respect to the wavelength. Therefore, the resolution of refractive index sensing can be low as the order of 10^{-6} RIU [39]. Different from SPPs and BSWs, the dispersion relation of TPPs lies inside the light cone. In other words, TPPs can be directly excited by the electromagnetic waves incident from the air without additional coupling components or coupling structures [44–48]. Nonetheless, metal layers with inevitable absorption are required to obtain TPPs. Such inevitable absorption of metal layers limits the resolution of refractive index sensing based on ellipsometric phase change of TPPs [40].

As a kind of lossless micro-structures, all-dielectric 1-D PhCs have received enormous attention since they play an important role in nano-optics [49–53]. Owing to the multiple scattering, the reflection phase at band edges in 1-D PhCs changes insensitively with respect to the wavelength while that within the photonic bandgap (PBG) changes smoothly with respect to the wavelength [54–56]. To the best of our knowledge, ellipsometric phase at band edges in 1-D PhCs has *not* been studied yet. In this paper, we realize dramatic ellipsometric phase change at band edges in a 1-D PhC for oblique incidence. Since the axial symmetry of the system for oblique incidence is broken, the wavelengths of band edges in the 1-D PhC for TM and TE polarizations are different. Therefore, at the wavelength of the band edge in the 1-D PhC for TM or TE polarization, the ellipsometric phase changes dramatically with respect to the wavelength. By virtue of the dramatic ellipsometric phase change at the long-wavelength band edge, we achieve ultra-sensitive refractive index sensing at near-infrared wavelengths. The minimal resolution reaches 9.28×10^{-8} RIU. Compared with SPP-, BSW- and TPP-based sensitive refractive index sensing, ultra-sensitive refractive index sensing achieved in this work does *not* require any additional coupling component, coupling structure, or metal. According to the continuity relation of tangential component of wave vector, the state of band edge can be directly excited from the electromagnetic wave incident from the air. The designed 1-D PhC is composed of alternating silicon (Si) and silicon oxide (SiO_2) layers, which can be easily fabricated via the current electron-beam vacuum deposition [52] or the magnetron sputtering techniques [57]. Such ultra-sensitive refractive index sensor would possess applications in monitoring temperature, humidity, pressure, and concentration of biological analytes.

This paper is organized as follows. In Sec. 2, we realize dramatic ellipsometric phase change at the band edges in an all-dielectric 1-D PhC and explain the underlying reason. In Sec. 3, we utilize the dramatic ellipsometric phase change to achieve ultra-sensitive refractive index sensing. In Sec. 4, we show an application of the refractive index sensing: measuring the concentration of sucrose. Finally, the conclusions are given in Sec. 5.

2. Dramatic ellipsometric phase change at band edge in 1-D PhC

Figure 1 gives the schematic of the proposed ultra-sensitive refractive index sensor. The 1-D PhC $(AB)^N$ is composed of alternating Si and SiO_2 layers. Simultaneously considering the minimal resolution of refractive index sensing and the difficulty of the fabrication process of the 1-D PhC, the number of periods of the 1-D PhC is selected to be N = 15 (details can be seen from Sec. 3). The incident medium is set to be the air and the exit medium (sensing medium) is set to be the

Optics EXPRESS

biosolution ($n_{\mathrm{Bio}} = 1.33$). Suppose that a plane wave launches into the 1-D PhC with an incident angle θ.

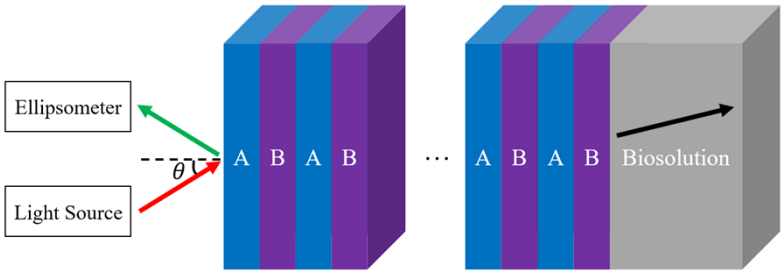

Fig. 1. Schematic of the proposed ultra-sensitive refractive index sensor. The 1-D PhC $(\mathrm{AB})^{15}$ is composed of alternating Si and SiO_2 layers. The incident medium is set to be the air and the exit medium (sensing medium) is set to be the biosolution.

Figures 2(a) and 2(b) give the measured data (black circles, extracted from Ref. [58]) of the real parts of the refractive indices of Si and SiO_2 [i.e., $\mathrm{Re}(n_{\mathrm{A}})$ and $\mathrm{Re}(n_{\mathrm{B}})$] as functions of the wavelength, respectively. Then, we utilize the polynomial functions to fit the real parts of the refractive indices of Si and SiO_2. The corresponding fitting curves are also shown by the blue solid lines. The fitting polynomial functions can be expressed as

$$Re(n_{\mathrm{A}}) = -1.1831\lambda^3 + 5.2301\lambda^2 - 7.7643\lambda + 7.3651, \tag{1}$$

$$Re(n_{\mathrm{B}}) = -0.011934\lambda + 1.4625, \tag{2}$$

where λ represents the wavelength in units of micrometer. Considering the material losses during the fabrication process, the imaginary parts of the refractive indices of Si and SiO_2 thin films within the wavelength range of interest are chosen to be $\kappa_{\mathrm{A}} = \mathrm{Im}(n_{\mathrm{A}}) = 1\times10^{-4}$ [59] and $\kappa_{\mathrm{B}} = \mathrm{Im}(n_{\mathrm{B}}) = 1.2\times10^{-5}$ [60], respectively. The thicknesses of Si and SiO_2 layers satisfy the quarter-wavelength condition $\mathrm{Re}(n_{\mathrm{A}})d_{\mathrm{A}} = \mathrm{Re}(n_{\mathrm{B}})d_{\mathrm{B}} = \lambda_{\mathrm{Brg}}/4 = c/(4f_{\mathrm{Brg}})$, where the Bragg wavelength is set to be $\lambda_{\mathrm{Brg}} = 1140$ nm (the corresponding Bragg frequency is $f_{\mathrm{Brg}} = 263.16$ THz). Notice that the Bragg wavelength can be selected to be another value as long as the PBG (along with its band edges) can occur since what we utilize to achieve ultra-sensitive refractive index sensing is the resonance of the band edge of the PBG. Since the quarter-wavelength condition is satisfied, the Bragg frequency is the center frequency of the PBG when the dispersion effects of the refractive indices of Si and SiO_2 are ignored [61]. However, here we consider the dispersion effects of the refractive indices of Si and SiO_2, the Bragg frequency slightly deviates from the center frequency of the PBG ($f_{\mathrm{center}} = 269.93$ THz). Hence, the thicknesses of Si and SiO_2 layers can be calculated as $d_{\mathrm{A}} = 80.1$ nm and $d_{\mathrm{B}} = 196.7$ nm, respectively.

According to the transfer matrix method [62], we calculate the reflectance spectrum and the reflection phase spectrum (in deg) of the 1-D PhC $(\mathrm{AB})^{15}$ at normal incidence in Figs. 3(a) and 3(b), respectively. Owing to the axial symmetry of the system, the TM reflectance spectrum (or the TM reflection phase spectrum) is identical to the TE reflectance spectrum (or the TE reflection phase spectrum) [49]. Clearly, a PBG is opened around the Bragg wavelength $\lambda_{\mathrm{Brg}} = 1140$ nm. The short- and the long-wavelength band edges are located at 867.5 and 1546.0 nm, respectively. Notice that the positions of the band edges are estimated using the reflectance dips nearest the PBG. Around the short- and the long-wavelength band edges, the reflection phase changes intensively due to the multiple scattering. In contrast, with the PBG, the reflection phase changes smoothly. In the following, we will utilize such intensive reflection phase change around the band edge to achieve dramatic ellipsometric phase change at the band edge for the case of oblique incidence.

Optics EXPRESS

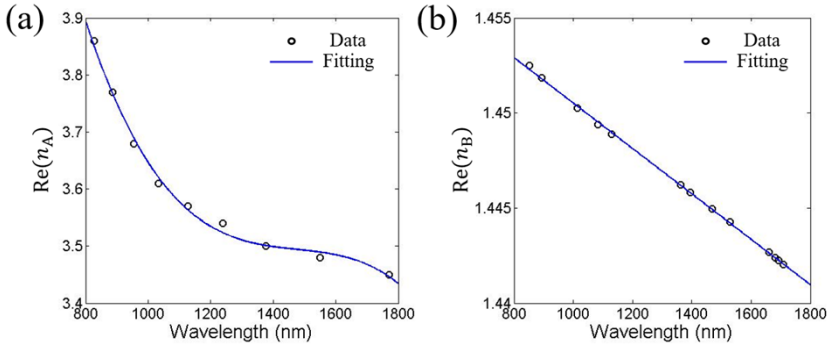

Fig. 2. Real parts of the refractive indices of (a) Si and (b) SiO_2 as functions of the wavelength. The black circles represent the measured data extracted from Ref. [58]. The blue solid lines represent the polynomial fitting curves.

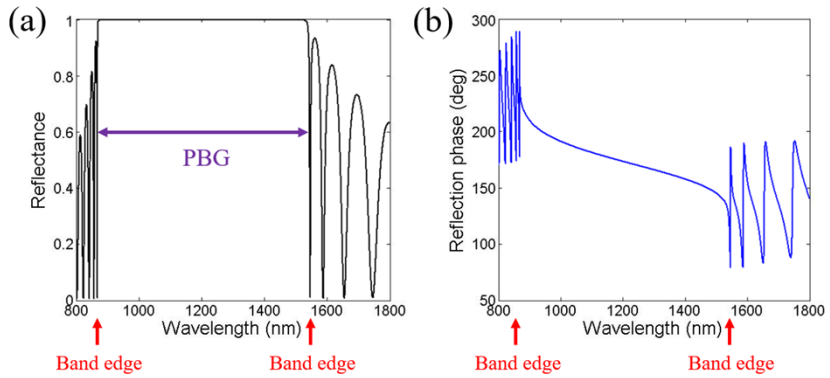

Fig. 3. (a) Reflectance and (b) reflection phase spectra (in deg) of the 1-D PhC $(AB)^{15}$ at normal incidence. The refractive index of the biosolution is set to be $n_{Bio} = 1.33$.

For the case of oblique incidence, the axial symmetry of the system is broken. Therefore, the TE reflectance spectrum (or the TE reflection phase spectrum) becomes distinguishable from the TM reflectance spectrum (or the TM reflection phase spectrum). Figure 4 gives the reflectance spectrum of the 1-D PhC $(AB)^{15}$ as a function of the incident angle for TM and TE polarizations. The left half represents TM polarization while the right half represents TE polarization. The black color represents unity reflectance while the white color represents zero reflectance. One can see that the TE reflectance spectrum is indeed different from the TM reflectance spectrum at oblique incidence. Specifically, as the incident angle increases from 0° to 60°, the short-wavelength band edge for TM polarization shifts from 867.5 to 819.4 nm while that for TE polarization shifts from 867.5 to 765.6 nm. At the same time, the long-wavelength band edge for TM polarization shifts from 1546.0 to 1222.8 nm while that for TE polarization shifts from 1546.0 to 1472.9 nm. The wavelength difference between the band edges for TM and TE polarizations gives rise to the reflection phase difference between the TM and TE polarizations. Without losing the generality, we only focus on the long-wavelength band edge.

Next, we select two typical incident angles $\theta_1 = 15°$ and $\theta_2 = 30°$ to observe the ellipsometric phase. Figures 5(a) gives the reflectance spectra of the 1-D PhC $(AB)^{15}$ at $\theta_1 = 15°$ for TM and TE polarizations. As demonstrated, the long-wavelength band edge for TM polarization is located at 1518.3 nm (shown by point A) while that for TE polarization is located at 1539.6 nm (shown by point B). The wavelength difference of the long-wavelength band edge for TM and

Optics EXPRESS

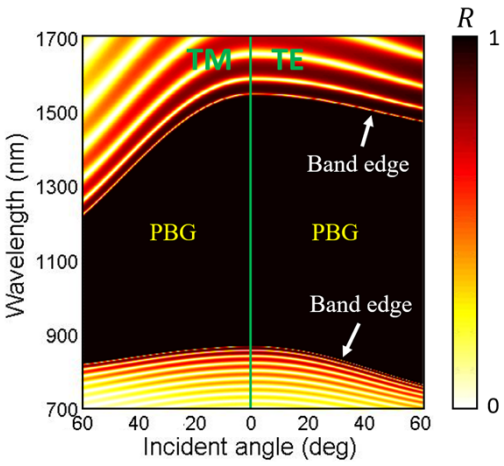

Fig. 4. Reflectance spectrum of the 1-D PhC $(AB)^{15}$ as a function of the incident angle for TM and TE polarizations. The left half represents TM polarization while the right half represents TE polarization.

TE polarizations is 21.3 nm. Figure 5(c) gives the reflection phase spectra (in deg) of the 1-D PhC $(AB)^{15}$ at $\theta_1 = 15°$ for TM and TE polarizations. Clearly, around the long-wavelength band edge for TM or TE polarization, the reflection phase changes intensively. In contrast, at other wavelengths, the reflection phase changes smoothly. Two ellipsometric parameters (ellipsometric amplitude Ψ and the ellipsometric phase Δ) satisfy the following equation [39]

$$\frac{r_{\mathrm{TM}}}{r_{\mathrm{TE}}} = \tan\Psi e^{i\Delta}, \tag{3}$$

where r_{TM} and r_{TE} represent the reflection coefficients for TM and TE polarizations, respectively. Furthermore, the reflection coefficients for TM and TE polarizations can be expressed as

$$r_{\mathrm{TM}} = |r_{\mathrm{TM}}|e^{i\varphi_{\mathrm{TM}}}, \tag{4}$$

$$r_{\mathrm{TE}} = |r_{\mathrm{TE}}|e^{i\varphi_{\mathrm{TE}}}, \tag{5}$$

where φ_{TM} and φ_{TE} represent the reflection phases for TM and TE polarizations, respectively. Substituting Eqs. (4) and (5) into Eq. (3), one can obtain the expressions of two ellipsometric parameters

$$\Psi = \arctan\frac{|r_{\mathrm{TM}}|}{|r_{\mathrm{TE}}|}, \tag{6}$$

$$\Delta = \varphi_{\mathrm{TM}} - \varphi_{\mathrm{TE}}. \tag{7}$$

Therefore, the ellipsometric phase Δ is the reflection phase difference between TM and TE polarizations. Figure 5(e) gives the ellipsometric phase spectrum (in deg) of the 1-D PhC $(AB)^{15}$ at $\theta_1 = 15°$. Interestingly, the ellipsometric phase changes dramatically at both the long-wavelength band edges for TM and TE polarizations. The reason can be explained as follows. At the long-wavelength band edge for TM polarization, the reflection phase for TM polarization changes intensively while that for TE polarization changes smoothly. Hence, the ellipsometer phase $\Delta = \varphi_{\mathrm{TM}} - \varphi_{\mathrm{TE}}$ changes dramatically. Similarly, at the long-wavelength band edge for TE polarization, the reflection phase for TM polarization changes smoothly while that for TE polarization changes intensively. Hence, the ellipsometer phase $\Delta = \varphi_{\mathrm{TM}} - \varphi_{\mathrm{TE}}$ also changes dramatically.

Optics EXPRESS

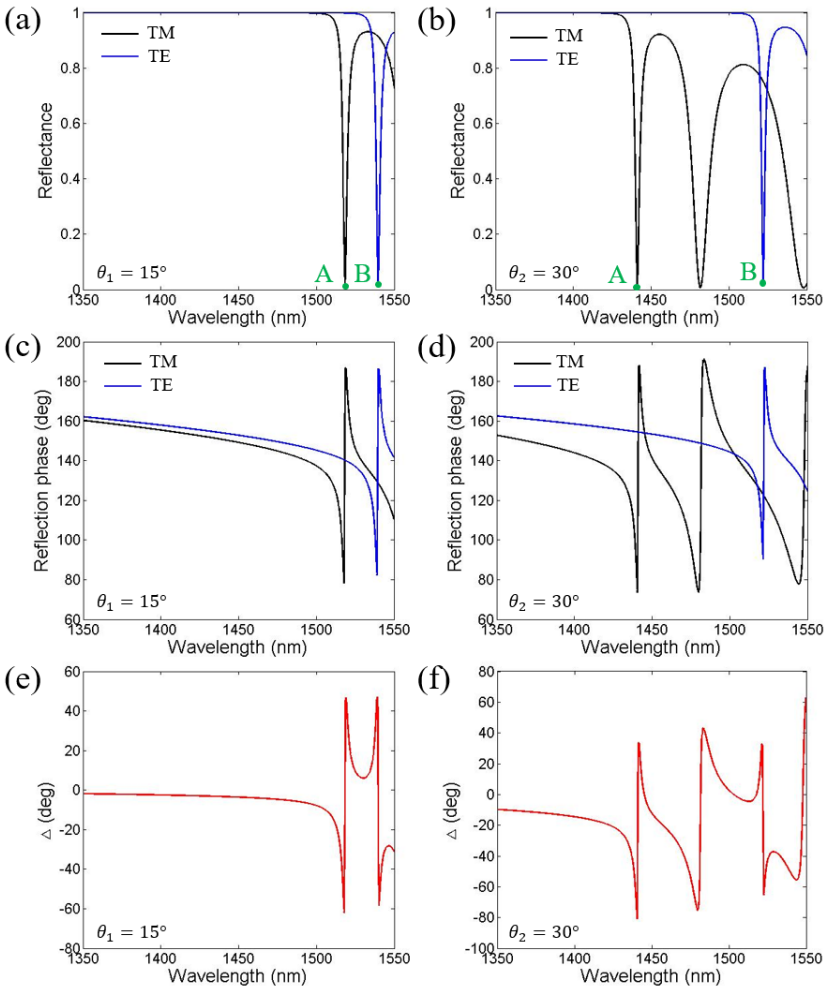

Fig. 5. (a) Reflectance, (c) reflection phase (in deg) and (e) ellipsometric phase (in deg) spectra of the 1-D PhC $(AB)^{15}$ at $\theta_1 = 15°$. (b) Reflectance, (d) reflection phase (in deg) and (f) ellipsometric phase (in deg) spectra of the 1-D PhC $(AB)^{15}$ at $\theta_2 = 30°$.

Optics EXPRESS

Similarly, Fig. 5(b) gives the reflectance spectra of the 1-D PhC $(AB)^{15}$ at $\theta_2 = 30°$ for TM and TE polarizations. As demonstrated, the long-wavelength band edge for TM polarization is located at 1441.1 nm (shown by point A) while that for TE polarization is located at 1522.0 nm (shown by point B). The wavelength difference of the long-wavelength band edge for TM and TE polarizations at $\theta_2 = 30°$ reaches 80.9 nm, which is larger than that at $\theta_1 = 15°$. Figure 5(d) gives the reflection phase spectra (in deg) of the 1-D PhC $(AB)^{15}$ at $\theta_2 = 30°$ for TM and TE polarizations. Clearly, around the long-wavelength band edge for TM or TE polarization, the reflection phase changes intensively. In contrast, at other wavelengths, the reflection phase changes smoothly. Figure 5(f) gives the ellipsometric phase spectrum (in deg) of the 1-D PhC $(AB)^{15}$ at $\theta_2 = 30°$. Similar to Fig. 5(e), the ellipsometric phase changes dramatically at both the long-wavelength band edges for TM and TE polarizations. Such dramatic ellipsometric phase change at the long-wavelength band edge can be utilized to achieve ultra-sensitive refractive index sensing.

3. Ultra-sensitive refractive index sensing enabled by dramatic ellipsometric phase change

In this section, we utilize the dramatic ellipsometric phase change at the long-wavelength band edge for TM polarization in Sec. 2 to achieve ultra-sensitive refractive index sensing. It is known that as the first derivative (absolute value) of the ellipsometric phase with respective to the wavelength becomes larger, the sensitivity of the refractive index sensing becomes more sensitive [27]. As the first derivative (absolute value) of the ellipsometric phase with respective to the wavelength becomes larger, the ellipsometric phase at a fixed wavelength changes more dramatically with the refractive index of the biosolution, giving rise to a larger sensitivity and a smaller resolution. The first derivative (absolute value) of the ellipsometric phase with respective to the wavelength can be expressed as

$$F = \left|\frac{\mathrm{d}\Delta}{\mathrm{d}\lambda}\right|. \tag{8}$$

For a fixed incident angle, we calculate the first derivative (absolute value) F as a function of the wavelength and then obtain the maximal first derivative (absolute value) $F_{\max}$. Figure 6 gives the relationship between the maximal first derivative (absolute value) $F_{\max}$ (in deg/nm) and the incident angle (in deg). As demonstrated, as the incident angle increases from 45.0° to 57.0°, the maximal first derivative (absolute value) $F_{\max}$ increases from 6.00×10^2 to 8.79×10^4. As the incident angle increases from 57.0° to 70.0°, the maximal first derivative (absolute value) $F_{\max}$ decreases from 8.79×10^4 to 3.45×10^2. Therefore, the maximal first derivative (absolute value) reaches its maximum 8.79×10^4 at $\theta_0 = 57.0°$. To achieve ultra-sensitive refractive index sensing, we select the incident angle as $\theta_0 = 57.0°$ in the following.

To assess the performance of the refractive index sensing, we calculate the ellipsometric phase spectra (in deg) at the incident angle $\theta_0 = 57.0°$ with different refractive indices of the sensing medium (i.e., the biosolution) $n_{\mathrm{Bio}} = 1.33$, 1.335 and 1.34 in Fig. 7(a). Owing to the ultra-large first derivative (absolute value), the ellipsometric phase is ultra-sensitive to the refractive index of the biosolution at the long-wavelength band edge. Specifically, as the refractive index of the biosolution slightly increases from 1.33 to 1.34, the ellipsometric phase at the fixed wavelength $\lambda_0 = 1243.35$ nm dramatically increases from –162.0° to –154.0°. Figure 7(b) further gives the ellipsometric phase (in deg) at the fixed wavelength $\lambda_0 = 1243.35$ nm and the incident angle $\theta_0 = 57.0°$ as a function of the refractive index of the biosolution. As the refractive index of the biosolution increases from 1.33 to 1.43, the ellipsometric phase dramatically increases from –161.0° to 1.6°. The total ellipsometric phase change reaches 162.6°.

Optics EXPRESS

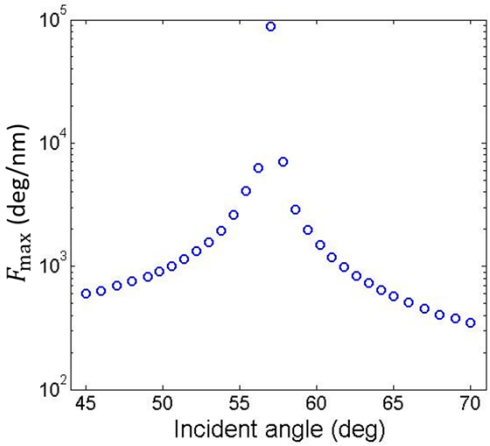

Fig. 6. Relationship between the maximal first derivative (absolute value) $F_{\max}$ (in deg/nm) and the incident angle (in deg).

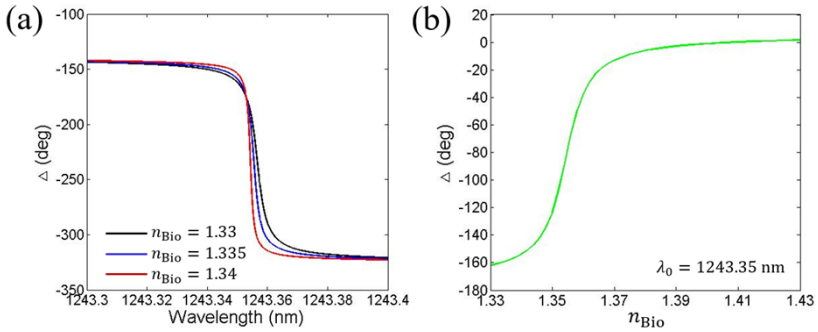

Fig. 7. (a) Ellipsometric phase spectra (in deg) at the incident angle $\theta_0 = 57.0°$ with different refractive indices of the biosolution $n_{\text{Bio}} = 1.33$, 1.335 and 1.34. (b) Ellipsometric phase (in deg) at the fixed wavelength $\lambda_0 = 1243.35$ nm and the incident angle $\theta_0 = 57.0°$ as a function of the refractive index of the biosolution.

The sensitivity of the refractive index sensor based on ellipsometric change can be determined by [63]

$$S = \left| \frac{\mathrm{d}\Delta}{\mathrm{d}n_{\text{Bio}}} \right|. \tag{9}$$

According to Eq. (9), we calculate the sensitivity (in deg/RIU) at the fixed wavelength $\lambda_0 = 1243.35$ nm and the incident angle $\theta_0 = 57.0°$ as a function of the refractive index of the biosolution, as shown in Fig. 8(a). Clearly, as the refractive index of the biosolution increases from 1.33 to 1.354, the sensitivity increases from 4.89×10^2 to 1.08×10^4 deg/RIU. As the refractive index of the biosolution continues to increase from 1.354 to 1.43, the sensitivity decreases from 1.08×10^4 to 5.19×10^1 deg/RIU. The maximal sensitivity reaches 1.08×10^4 deg/RIU.

Under the current ellipsometric phase measuring technique, a realistically achievable limit of the ellipsometric phase noise is $\delta\Delta = 0.001°$ [64]. Therefore, the resolution of the refractive index sensing (i.e., δn) can be calculated by [65]

$$\delta n = \frac{\delta\Delta}{S}. \tag{10}$$

Optics EXPRESS

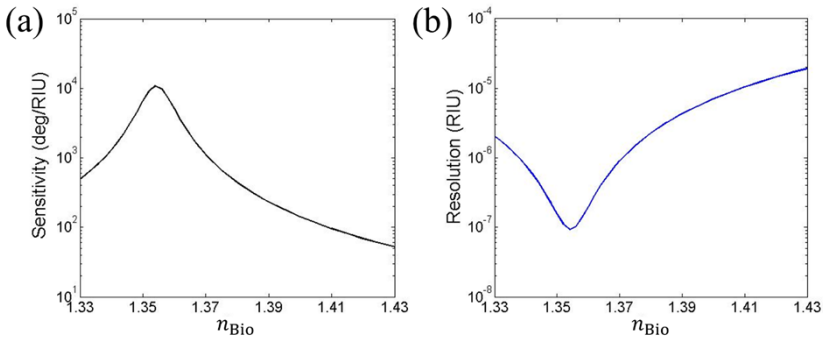

Fig. 8. (a) Sensitivity (in deg/RIU) and (b) resolution (in RIU) at the fixed wavelength $\lambda_0 = 1243.35$ nm and the incident angle $\theta_0 = 57.0°$ as functions of the refractive index of the biosolution.

One can see that the minimal resolution δn is inversely proportional to the sensitivity S. Once the realistically achieved limit of the ellipsometric phase noise $\delta\Delta$ is determined, the minimal resolution δn is completely determined by the sensitivity S. According to Eq. (10), we calculate the resolution of the refractive index sensing (in RIU) at the fixed wavelength $\lambda_0 = 1243.35$ nm and the incident angle $\theta_0 = 57.0°$ as a function of the refractive index of the biosolution, as shown in Fig. 8(b). Clearly, as the refractive index of the biosolution increases from 1.33 to 1.354, the resolution decreases from 2.05×10^{-6} to 9.28×10^{-8} RIU. As the refractive index of the biosolution continues to increase from 1.354 to 1.43, the resolution increases from 9.28×10^{-8} to 1.93×10^{-5} RIU. The minimal resolution reaches 9.28×10^{-8} RIU.

As we illustrated in Sec. 2, as the number of periods N increases, the resonance of the long-wavelength band edge becomes stronger. Hence, the minimal resolution becomes smaller. Table 1 gives the minimal resolution of the 1-D PhCs $(AB)^N$ with different numbers of periods N = 5, 10 and 15. It can be seen that the minimal resolutions for N = 5, 10 and 15 are 6.81×10^{-7}, 2.55×10^{-7} and 9.28×10^{-8} RIU, respectively. As the number of periods N increases, the minimal resolution becomes smaller. However, the increase in the number of periods N will increase the difficulty of the fabrication process of the 1-D PhC. Simultaneously considering the minimal resolution and the difficulty of the fabrication process, we finally select the number of periods N = 15.

Table 1. Minimal resolution of the 1-D PhCs $(AB)^N$ with different numbers of periods N = 5, 10 and 15

Number of periods N	Incident angle θ_0 (deg)	Wavelength λ_0 (nm)	Minimal resolution (RIU)
5	53.0	1371.80	6.81×10^{-7}
10	54.5	1277.12	2.55×10^{-7}
15	57.0	1243.35	9.28×10^{-8}

Finally, we compare the performance of the refractive index sensing in this work with those in the reported works based on various mechanisms (SPPs [25,26], BSWs [32,33] and ellipsometric phase change [39]), as shown in Table 2. One can see that the refractive index sensing achieved in this work does *not* require any coupling component, coupling structure, or metal while possessing the smallest resolution. The ultra-sensitive refractive index sensing achieved in this work would be utilized in ultra-sensitively monitoring temperature, humidity, pressure, and concentration of biological analytes.

Optics EXPRESS

Table 2. Comparison between the performance of the refractive index sensing achieved in this work and those in the reported works based on various mechanisms

	Mechanism	Need coupling component or coupling structure?	Need metal?	Minimal resolution (RIU)
Ref. [25]	SPP	Yes	Yes	2.2×10^{-5}
Ref. [26]	SPP	Yes	Yes	3.5×10^{-6}
Ref. [32]	BSW	Yes	No	5.9×10^{-5}
Ref. [33]	BSW	Yes	No	$\sim10^{-5}$
Ref. [39]	Ellipsometric phase change	No	Yes	$\sim10^{-6}$
This work	Ellipsometric phase change	No	No	9.28×10^{-8}

4. Application: measuring concentration of sucrose

In this section, we show an application of the refractive index sensing: measuring the concentration of sucrose. The biosolution in Fig. 1 is selected to be sucrose. Figure 9 gives the measured data (black circles, extracted from Ref. [66]) of the refractive index of sucrose n_{Bio} as a function of the concentration. Then, we utilize a linear function (shown by blue solid line) to fit the refractive index of sucrose. The fitting function can be expressed as

$$n_{\mathrm{Bio}} = 0.016286C + 1.334, \tag{11}$$

where C represents the concentration of sucrose in units of g/L.

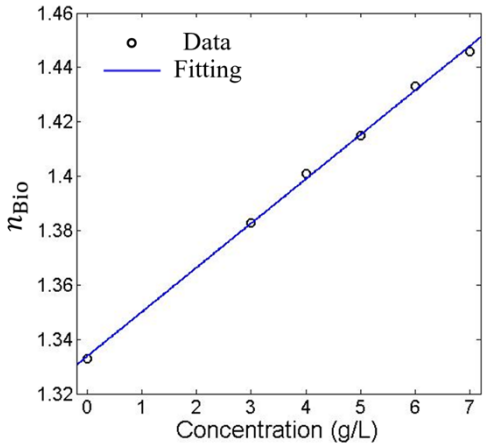

Fig. 9. Refractive index of sucrose as a function of the concentration. The black circles represent the measured data extracted from Ref. [66]. The blue solid line represents the linear fitting curves.

Figure 10(a) gives the ellipsometric phase spectra (in deg) at the incident angle $\theta_0 = 57.0°$ with different concentrations of sucrose $C = 0$, 0.3 and 0.6 g/L. As the concentration of sucrose slightly increases from 0 to 0.6 g/L, the ellipsometric phase at the fixed wavelength $\lambda_0 = 1243.35$ nm dramatically increases from –159.7° to –147.6°. Figure 10(b) further gives the ellipsometric phase (in deg) at the fixed wavelength $\lambda_0 = 1243.35$ nm and the incident angle $\theta_0 = 57.0°$ as a function of the concentration of sucrose. As the concentration of sucrose increases from 0 to 5 g/L, the ellipsometric phase dramatically increases from –159.7° to 0.7°. The total ellipsometric phase change reaches 160.4°.

Optics EXPRESS

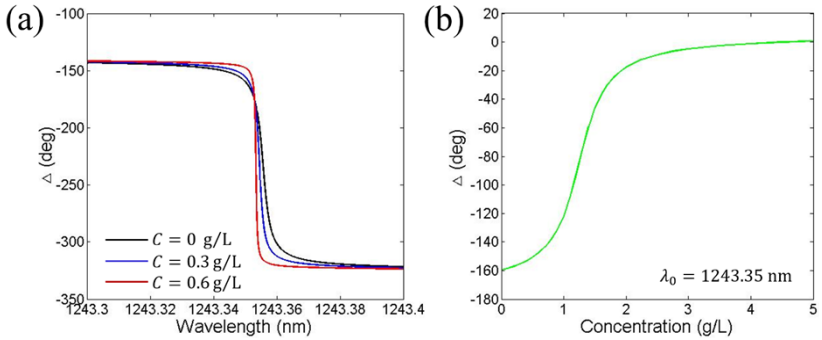

Fig. 10. (a) Ellipsometric phase spectra (in deg) at the incident angle $\theta_0 = 57.0°$ with different concentrations of sucrose $C = 0$, 0.3 and 0.6 g/L. (b) Ellipsometric phase (in deg) at the fixed wavelength $\lambda_0 = 1243.35$ nm and the incident angle $\theta_0 = 57.0°$ as a function of the concentration of sucrose.

The sensitivity of the concentration of sucrose based on ellipsometric change can be determined by

$$S = \left|\frac{d\Delta}{dC}\right|. \tag{12}$$

According to Eq. (12), we calculate the sensitivity (in deg·L/g) at the fixed wavelength $\lambda_0 = 1243.35$ nm and the incident angle $\theta_0 = 57.0°$ as a function of the concentration of sucrose, as shown in Fig. 11(a). Clearly, as the concentration of sucrose increases from 0 to 1.2 g/L, the sensitivity increases from 1.12×10^1 to 1.72×10^2 deg·L/g. As the concentration of sucrose continues to increase from 1.2 to 5 g/L, the sensitivity decreases from 1.72×10^2 to $1.30\times10°$ deg·L/g. The maximal sensitivity reaches 1.72×10^2 deg·L/g.

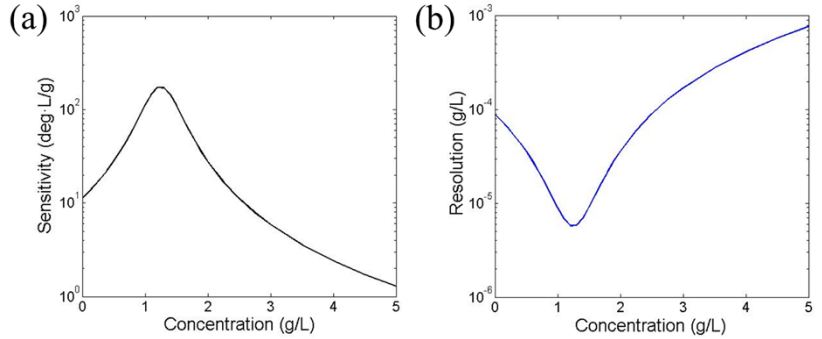

Fig. 11. (a) Sensitivity (in deg·L/g) and (b) resolution (in g/L) at the fixed wavelength $\lambda_0 = 1243.35$ nm and the incident angle $\theta_0 = 57.0°$ as functions of the concentration of sucrose.

Under the current ellipsometric phase measuring technique, a realistically achievable limit of the ellipsometric phase noise is $\delta\Delta = 0.001°$ [64]. Therefore, the resolution of the concentration of sucrose (i.e., δC) can be calculated by

$$\delta C = \frac{\delta\Delta}{S}. \tag{13}$$

According to Eq. (13), we calculate the resolution of the concentration of sucrose (in g/L) at the fixed wavelength $\lambda_0 = 1243.35$ nm and the incident angle $\theta_0 = 57.0°$ as a function of the

Optics EXPRESS

concentration of sucrose, as shown in Fig. 11(b). Clearly, as the concentration of sucrose increases from 0 to 1.2 g/L, the resolution decreases from 8.94×10^{-5} to 5.80×10^{-6} g/L. As the concentration of sucrose continues to increase from 1.2 to 5 g/L, the resolution increases from 5.80×10^{-6} to 7.70×10^{-4} g/L. The minimal resolution reaches 5.80×10^{-6} g/L.

5. Conclusion

In summary, we design an ultra-sensitive refractive index sensor based on the dramatic ellipsometric phase change at the long-wavelength band edge in an all-dielectric 1-D PhC. Assisted by the dramatic ellipsometric phase change at the long-wavelength band edge, the minimal resolution of the designed sensor reaches 9.28×10^{-8} RIU. Compared with conventional SPP-, BSW- and TPP-based sensitive refractive index sensors, the designed ultra-sensitive refractive index sensor does *not* require any additional coupling component, coupling structure, or metal. Such ultra-sensitive refractive index sensor would possess applications in monitoring temperature, humidity, pressure, and concentration of biological analytes.

Funding. National Natural Science Foundation of China (12104105, 61805064); Science and Technology Program of Guangzhou (202102020571); Shanghai Pujiang Program (20PJ1412200); Start-up Funding of Guangdong Polytechnic Normal University (2021SDKYA033).

Disclosures. The authors declare that there are no conflicts of interest related to this article.

Data availability. Data underlying the results presented in this paper are available from the corresponding authors upon reasonable request.

References

1. C. E. Lee, R. A. Atkins, and H. F. Taylor, "Performance of a fiber-optic temperature sensor from −200 to 1050°C," Opt. Lett. **13**(11), 1038–1040 (1988).
2. V. Kavungal, G. Farrell, Q. Wu, A. K. Mallik, and Y. Semenova, "Thermo-optic tuning of a packaged whispering gallery mode resonator filled with nematic liquid crystal," Opt. Express **26**(7), 8431–8442 (2018).
3. F. Wu, J. Wu, Z. Guo, H. Jiang, Y. Sun, Y. Li, J. Ren, and H. Chen, "Giant Enhancement of the Goos-Hänchen Shift Assisted by Quasibound States in the Continuum," Phys. Rev. Appl. **12**(1), 014028 (2019).
4. X. Wang, M. Sang, W. Yuan, Y. Nie, and H. Luo, "Optical relative humidity sensing based on oscillating wave-enhanced Goos-Hänchen shift," IEEE Photon. Technol. Lett. **28**(3), 264–267 (2016).
5. M. Gryga, D. Ciprian, L. Gembalova, and P. Hlubina, "Sensing based on Bloch surface wave and self-referenced guided mode resonances employing a one-dimensional photonic crystal," Opt. Express **29**(9), 12996–13010 (2021).
6. M. Ohkawa, K. Hasebe, S. Sekine, and T. Sato, "Relationship between sensitivity and waveguide position on the diaphragm in integrated optic pressure sensors based on the elasto-optic effect," Appl. Opt. **41**(24), 5016–5021 (2002).
7. S. Jena, R. B. Tokas, S. Thakur, and D. V. Udupa, "Tunable mirrors and filters in 1D photonic crystals containing polymers," Physica E **114**, 113627 (2019).
8. T. Weiss, M. Mesch, M. Schäferling, H. Giessen, W. Langbein, and E. A. Muljarov, "From dark to bright: First-order perturbation theory with analytical mode normalization for plasmonic nanoantenna arrays applied to refractive index sensing," Phys. Rev. Lett. **116**(23), 237401 (2016).
9. K. V. Sreekanth, Y. Alapan, M. ElKabbash, E. Ilker, M. Hinczewski, U. A. Gurkan, A. De Luca, and G. Strangi, "Extreme sensitivity biosensing platform based on hyperbolic metamaterials," Nat. Mater. **15**(6), 621–627 (2016).
10. A. Panda, P. D. Pukhrambam, F. Wu, and W. Belhadj, "Graphene-based 1D defective photonic crystal biosensor for real-time defection of cancer cells," Eur. Phys. J. Plus **136**(8), 809 (2021).
11. S. Romano, G. Zito, S. Torino, G. Calafiore, E. Penzo, G. Coppola, S. Cabrini, I. Rendina, and V. Mocella, "Label-free sensing of ultralow-weight molecules with all-dielectric metasurfaces supporting bound states in the continuum," Photon. Res. **6**(7), 726–733 (2018).
12. B. Wan, Z. Zhou, Y. Xu, and H. Zhang, "A theoretical proposal for a refractive index and angle sensor based on one-dimensional photonic crystals," IEEE Sensors J. **21**(1), 331–338 (2020).
13. S. E.-S. A. El-Ghany, W. M. Nouman, Z. S. Matar, Z. A. Zaky, and A. H. Aly, "Optimized bio-photonic sensor using 1D-photonic crystals as a blood hemoglobin sensor," Phys. Scr. **96**(3), 035501 (2021).
14. A. S. Kostyukov, A. E. Ershov, R. G. Bikbaev, V. S. Gerasimov, I. L. Rasskazov, S. V. Karpov, and S. P. Polyutov, "Substrate-mediated lattice Kerker effect in Al metasurfaces," J. Opt. Soc. Am. B **38**(9), C78–C83 (2021).
15. M. Kumar, K. B. Thapa, and P. Singh, "Long-range surface plasmon resonance biosensors with cytop/Al/Perovskite and cytop/Al/MoS_2 configurations," Phys. Scr. **97**(5), 055501 (2022).
16. D. N. Maksimov, V. S. Gerasimov, A. A. Bogdanov, and S. P. Polyutov, "Enhanced sensitivity of an all-dielectric refractive index sensor with an optical bound state in the continuum," Phys. Rev. A **105**(3), 033518 (2022).

Optics EXPRESS

17. J. G. Rivas, P. H. Kuttge, H. Bolivar, Kurz, and J. A. Sánchez-Gil, "Propagation of surface plasmon polaritons on semiconductor gratings," Phys. Rev. Lett. **93**(25), 256804 (2004).
18. A. V. Zayats, I. I. Smolyaninov, and A. A. Maradudin, "Nano-optics of surface plasmon polaritons," Phys. Rep. **408**(3-4), 131–314 (2005).
19. J. Zhang, L. Zhang, and W. Xu, "Surface plasmon polaritons: physics and applications," J. Phys. D: Appl. Phys. **45**(11), 113001 (2012).
20. S. Patskovsky, A. V. Kabashin, M. Meunier, and J. H. T. Luong, "Silicon-based surface plasmon resonance sensing with two surface plasmon polariton modes," Appl. Opt. **42**(34), 6905–6909 (2003).
21. I. I. Smolyaninov, J. Elliott, A. V. Zayats, and C. C. Davis, "Far-field optical microscopy with a nanometer-scale resolution based on the in-plane image magnification by surface plasmon polaritons," Phys. Rev. Lett. **94**(5), 057401 (2005).
22. M. Naheed and M. Faryad, "Excitation of surface plasmon-polariton waves at the interface of a metal and an isotropic chiral material in the prism-coupled configurations," Eur. Phys. J. Plus **135**(9), 724 (2020).
23. G. Nemova, A. V. Kabashin, and R. Kashyap, "Surface plasmon-polariton Mach-Zehnder refractive index sensor," J. Opt. Soc. Am. B **25**(10), 1673–1677 (2008).
24. H. Ni, L. Zhang, A. Ping, A. V. Krasavin, H. Ali, B. Ni, and J. Chang, "Dual-mode independent detection of pressure and refractive index by miniature grating-coupled surface plasmon sensor," Opt. Express **30**(4), 5758–5768 (2022).
25. Md.R. Hasan, S. Akter, A. A. Rifat, S. Rana, K. Ahmed, R. Ahmed, H. Subbaraman, and D. Abbott, "Spiral photonic crystal fiber-based dual-polarized surface plasmon resonance biosensor," IEEE Sensors J. **18**(1), 133–140 (2018).
26. F. Haider, R. A. Aoni, R. Ahmed, and A. E. Miroshnichenko, "Highly amplitude-sensitive photonic-crystal-fiber plasmonic sensor," J. Opt. Soc. Am. B **35**(11), 2816–2821 (2018).
27. Y. Li, T. Yang, S. Song, Z. Pang, G. Du, and S. Han, "Phase properties of Bloch surface waves and their sensing applications," Appl. Phys. Lett. **103**(4), 041116 (2013).
28. W. Kong, Z. Zheng, Y. Wan, S. Li, and J. Liu, "High-sensitivity sensing based on intensity-interrogated Bloch surface wave sensors," Sensor Actuat. B: Chem. **193**, 467–471 (2014).
29. R. Wang, H. Xia, D. Zhang, J. Chen, L. Zhu, Y. Wang, E. Yang, T. Zang, X. Wen, G. Zou, P. Wang, H. Ming, R. Badugu, and J. R. Lakowicz, "Bloch surface waves confined in one dimension with a single polymeric nanofiber," Nat. Commun. **8**(1), 14330 (2017).
30. P. Hlubina, M. Gryga, D. Ciprian, P. Pokorny, L. Gembalova, and J. Sobota, "High performance liquid analyte sensing based on Bloch surface wave resonances in the spectral domain," Opt. Laser Technol. **145**, 107492 (2022).
31. D. Ge, Y. Zhou, J. Shi, L. Zhang, and S. Zhu, "Highly sensitive refractive index sensor based on Bloch surface waves with lithium niobate film," Appl. Phys. A **128**(1), 53 (2022).
32. M. Gryga, D. Vala, P. Kolejak, L. Gembalova, D. Ciprian, and P. Hlubina, "One-dimensional photonic crystal for Bloch surface waves and radiation modes-based sensing," Opt. Mater. Express **9**(10), 4009–4022 (2019).
33. D. Niu, M. Zerrad, A. Lereu, A. Moreau, J. Lumeau, J. A. Zapien, A. Passian, V. Aubry, and C. Amra, "Excitation of Bloch surface waves in zero-admittance multilayers for high-sensitivity sensor applications," Phys. Rev. Appl. **13**(5), 054064 (2020).
34. Y. Wan, Z. Zheng, W. Kong, X. Zhao, Y. Liu, Y. Bian, and J. Liu, "Nearly three orders of magnitude enhancement of Goos-Hanchen shift by exciting Bloch surface wave," Opt. Express **20**(8), 8998–9003 (2012).
35. Y. Lang, Q. Liu, Q. Wang, X. Zhou, and G. Jia, "A method for measuring one-dimensional photonic crystal periodstructure-film thicknesses based on Bloch surface wave enhanced Goos-Hänchen shift," Chin. Phys. B (2022). [online]
36. M. Scaravilli, G. Castaldi, A. Cusano, and V. Galdi, "Grating-coupling-based excitation of Bloch surface waves for lab-on-fiber optrodes," Opt. Express **24**(24), 27771–27784 (2016).
37. C. Zhang, Q. Liu, X. Peng, Z. Ouyang, and S. Shen, "Sensitive THz sensing based on Fano resonance in all-polymetric Bloch surface wave structure," Nanophotonics **10**(15), 3879–3888 (2021).
38. W. Kong, S. Li, R. Meng, and X. Ni, "Wavelength manipulation in a grating metasurface loaded Bloch surface wave structure," Results Phys. **27**, 104496 (2021).
39. S. Huang, K. Chen, and S. Jeng, "Phase sensitive sensor on Tamm plasmon devices," Opt. Mater. Express **7**(4), 1267–1273 (2017).
40. Y. Tsurimaki, J. K. Tong, V. N. Boriskin, A. Semenov, M. I. Ayzatsky, Y. P. Machekhin, G. Chen, and S. V. Boriskina, "Topological engineering of interfacial optical Tamm states for highly sensitive near-singular-phase optical detection," ACS Photonics **5**(3), 929–938 (2018).
41. S. V. Boriskina and Y. Tsurimaki, "Sensitive singular-phase optical detection without phase measurements with Tamm plasmons," J. Phys.: Condens. Matter **30**(22), 224003 (2018).
42. J. Wu, F. Wu, C. Xue, Z. Guo, H. Jiang, Y. Sun, Y. Li, and H. Chen, "Wide-angle ultrasensitive biosensors based on edge states in heterostructures containing hyperbolic metamaterials," Opt. Express **27**(17), 24835–24846 (2019).
43. K. V. Sreekanth, S. Sreejith, S. Han, A. Mishra, X. Chen, H. Sun, C. T. Lim, and R. Singh, "Biosensing with the singular phase of an ultrathin metal-dielectric nanophotonic cavity," Nat. Commun. **9**(1), 369 (2018).
44. M. Kaliteevski, I. Iorsh, S. Brand, R. A. Abram, J. M. Chamberlain, A. V. Kavokin, and I. A. Shelykh, "Tamm plasmon-polaritons: possible electromagnetic states at the interface of a metal and a dielectric Bragg mirror," Phys. Rev. B **76**(16), 165415 (2007).

Optics EXPRESS

45. H. Lu, X. Gan, B. Jia, D. Mao, and J. Zhao, "Tunable high-efficiency light absorption of monolayer graphene via Tamm plasmon polaritons," Opt. Lett. **41**(20), 4743–4746 (2016).
46. X. Wang, X. Jiang, Q. You, J. Guo, X. Dai, and Y. Xiang, "Tunable and multichannel terahertz perfect absorber due to Tamm surface plasmons with graphene," Photon. Res. **5**(6), 536–542 (2017).
47. A. M. Vyunishev, R. G. Bikbaev, S. E. Svyakhovskiy, I. V. Timofeev, P. S. Pankin, S. A. Evlashin, S. Y. Vetrov, S. A. Myslivets, and V. G. Arkhipkin, "Broadband Tamm plasmon polariton," J. Opt. Soc. Am. B **36**(8), 2299–2305 (2019).
48. F. Wu, X. Wu, S. Xiao, G. Liu, and H. Li, "Broadband wide-angle multilayer absorber based on a broadband omnidirectional optical Tamm state," Opt. Express **29**(15), 23976–23987 (2021).
49. Y. Fink, J. N. Winn, S. Fan, C. Chen, J. Michel, J. D. Joannopoulos, and E. L. Thomas, "A dielectric omnidirectional reflector," Science **282**(5394), 1679–1682 (1998).
50. X. Kong, S. Liu, H. Zhang, C. Li, and B. Bian, "Omnidirectional photonic band gap of one-dimensional ternary plasma photonic crystals," J. Opt. **13**(3), 035101 (2011).
51. D. Qi, F. Chen, X. Wang, H. Luo, Y. Cheng, X. Niu, and R. Gong, "Effective strategy for visible-infrared compatible camouflage: surface graphical one-dimensional photonic crystal," Opt. Lett. **43**(21), 5323–5326 (2018).
52. F. Wang, Y. Z. Cheng, X. Wang, D. Qi, H. Luo, and R. Z. Gong, "Effective modulation of the photonic band gap based on Ge/ZnS one-dimensional photonic crystal at the infrared band," Opt. Mater. **75**, 373–378 (2018).
53. C. Song, H. Chen, Y. Wang, L. Jin, Y. Xu, L. Shi, Y. Zou, X. Ma, Y. Song, C. Wang, Y. Zhang, J. Lin, H. Zhang, H. Zhang, and J. Yao, "Gigahertz femtosecond laser-by a novel asymmetric one-dimensional photonic crystal saturable absorber device with defect layer," Nanophotonics **11**(12), 2939–2951 (2022).
54. J. D. Joannopoulos, S. G. Johnson, J. N. Winn, and R. D. Meade, *Photonic Crystals: Molding the Flow of Light* (Princeton University Press, 2008).
55. V. Popov, S. Tretyakov, and A. Novitsky, "Brewster effect when approaching exceptional points of degeneracy: epsilon-near-zero behavior," Phys. Rev. B **99**(4), 045146 (2019).
56. F. Wu, M. Chen, and S. Xiao, "Wide-angle polarization selectivity based on anomalous defect mode in photonic crystal containing hyperbolic metamaterials," Opt. Lett. **47**(9), 2153–2156 (2022).
57. S. Jena, R. B. Tokas, P. Sarkar, J. S. Misal, S. M. Haque, K. D. Rao, S. Thakur, and N. K. Sahoo, "Omnidirectional photonic band gap in magnetron sputtered TiO_2/SiO_2 one dimensional photonic crystal," Thin Solid Films **599**, 138–144 (2016).
58. E. Palik, *Handbook of Optical Constants of Solids I* (Academic Press, 1985).
59. M. A. Green and M. J. Keevers, "Optical properties of intrinsic silicon at 300 K," Prog. Photovoltaics **3**, 189–192 (1995).
60. A. Sinibaldi, R. Rizzo, G. Figliozzi, E. Descrovi, N. Danz, P. Munzert, A. Anopchenko, and F. Michelotti, "A full ellipsometric approach to optical sensing with Bloch surface waves on photonic crystals," Opt. Express **21**(20), 23331–23344 (2013).
61. A. Mouldi and M. Kanzari, "Design of microwave devices exploiting Fibonacci and hybrid periodic/Fibonacci one dimensional photonic crystals," Prog. Electromagn. Res. B **40**, 221–240 (2012).
62. P. Yeh, *Optical Waves in Layered Media* (Wiley, 1988).
63. T. Xue, W. Liang, Y. Li, Y. Sun, Y. Xiang, Y. Zhang, Z. Dai, Y. Duo, L. Wu, K. Qi, B. N. Shivananju, L. Zhang, X. Cui, H. Zhang, and Q. Bao, "Ultrasensitive detection of miRNA with an antimonene-based surface plasmon resonance sensor," Nat. Commun. **10**(1), 28 (2019).
64. Y. Huang, H. P. Ho, S. K. Kong, and A. V. Kabashin, "Phase-sensitive surface plasmon resonance biosensors: methodology, instrumentation and applications," Ann. Phys. **524**(11), 637–662 (2012).
65. F. Sohrabi, S. Saeidifard, and S. M. Hamidi, "Plasmonic structures for phase-sensitivity ellipsometry biosensing: a review," Opt. Quantum Electron. **53**(12), 710 (2021).
66. W. M. M. Yunus and A. A. Rahman, "Refractive index of solutions at high concentrations," Appl. Opt. **27**(16), 3341–3343 (1988).